JAMES | Journal of Advances in Modeling Earth Systems

RESEARCH ARTICLE
10.1029/2020MS002151

Vertical Structure of Ocean Mesoscale Eddies with Implications for Parameterizations of Tracer Transport

Z. Stanley[1], S. D. Bachman[2], and I. Grooms[1]

[1]Department of Applied Mathematics, University of Colorado, Boulder, Colorado, USA, [2]Climate and Global Dynamics Division, National Center for Atmospheric Research, Boulder, Colorado, USA

Key Points:
- The Gent–McWilliams (GM) coefficient matrix is diagnosed from an eddy-resolving simulation
- The vertical structure of GM is well modeled by a surface mode
- Horizontal anisotropy is crucial for obtaining a good fit

Correspondence to:
I. Grooms,
ian.grooms@colorado.edu

Citation:
Stanley, Z., Bachman, S. D., & Grooms, I. (2020). Vertical structure of ocean mesoscale eddies with implications for parameterizations of tracer transport. *Journal of Advances in Modeling Earth Systems*, *12*, e2020MS002151. https://doi.org/10.1029/2020MS002151

Received 23 APR 2020
Accepted 24 AUG 2020
Accepted article online 27 AUG 2020

Abstract The Gent–McWilliams parameterization is commonly used in global ocean models to model the advective component of tracer transport effected by unresolved mesoscale eddies. The vertical structure of the transfer coefficient in this parameterization is studied using data from a 0.1° resolution global ocean-ice simulation. The vertical structure is found to be well approximated by a baroclinic mode structure with no flow at the bottom, though horizontal anisotropy is crucial for obtaining a good fit. This vertical structure is motivated by reference to the vertical structure of mesoscale eddy velocity and density anomalies, which are also diagnosed from the data.

Plain Language Summary Ocean mesoscale eddies transport tracers like heat, salt, and dissolved carbon dioxide, inter alia. In numerical models where these eddies are not resolved, their effects need to be parameterized. This research addresses the vertical structure of a widely used parameterization, and connects the results to vertical structure of the eddies themselves.

1. Introduction

Ocean mesoscale eddies play an important role in transporting heat, salt, and biogeochemical dissolved tracers (McWilliams, 2013). Though global eddy-resolving calculations are becoming more commonplace (Qiu et al., 2018), the mesoscale eddy field remains largely unresolved in the majority of CMIP-class ocean models (Meijers, 2014). The ocean modeling community thus dedicates significant attention to developing techniques for representing the transport by these eddies.

Efforts are presently underway at some modeling centers to move toward eddy-permitting modeling as standard practice. As a result, many global ocean models are collectively run in a "gray zone" between eddy-free and eddy-permitting flow regimes. Appropriate techniques for parameterizing mesoscale eddies in these models include parameterizing them with Reynolds-averaged style methods (as in Hallberg, 2013; Visbeck et al., 1997) or modeling them with large-eddy-simulation (LES) style methods (as in Bachman et al., 2017; Fox-Kemper & Menemenlis, 2008). The subgrid-scale (SGS) eddy flux of a tracer C is

$$\boldsymbol{F}_C = \overline{\boldsymbol{u}C} - \overline{\boldsymbol{u}}\,\overline{C}, \tag{1}$$

where $\boldsymbol{u} = (u, v, w)$ is the velocity and $\bar{\cdot}$ is a spatial low-pass filter that extracts the part of a field that can be resolved on the model's grid. Reynolds-averaged parameterizations and LES models differ in their assumptions on further properties of the averaging operator; the definition of $\boldsymbol{F}_C$ used here is agnostic to the type of closure technique needed for a particular ocean model and so is appropriate for the ensuing discussion. For simplicity, we will also use "parameterization" as a blanket term to include all types of SGS closures.

The most common parameterization of mesoscale tracer transport employed in current non-eddying ocean models is a combination of isopycnal diffusion (Redi, 1982) and eddy-induced advection (Gent & McWilliams, 1990; Gent et al., 1995). Within this combined GM/Redi parameterization, the eddy tracer flux is modeled via a linear relationship to the large-scale tracer gradient (Griffies, 1998):

$$\boldsymbol{F}_C = J\nabla\overline{C}. \tag{2}$$

In this combined parameterization there is one $\mathbf{J}$ that applies for every tracer (Bachman et al., 2015). The symmetric part of the 3×3 matrix $\mathbf{J}$ corresponds to diffusion (or anti-diffusion, depending on the sign of the

eigenvalues), while the antisymmetric part corresponds to advection or "skew diffusion." In the Redi parameterization, the diffusive part is constructed so that it acts entirely along surfaces that minimize disturbances to stratification or energy (e.g., Griffies et al., 1998). Fox-Kemper et al. (2013) note that several thermodynamic variables can be used to define such surfaces (e.g., McDougall, 1987; Nycander, 2011; Young, 2010); here, for simplicity, we will use potential density (referenced to the surface) as this variable and the term "isopycnal" to describe the direction of transport by GM/Redi.

The divergence of the advective part of the eddy tracer flux is $\nabla \cdot (\boldsymbol{u}^* \bar{C})$ where the eddy-induced (or "bolus" or "quasi-Stokes") velocity $\boldsymbol{u}^*$ may be conveniently prescribed in terms of a vector $\boldsymbol{\Upsilon} = (\Upsilon^x, \Upsilon^y)$:

$$u^* = \partial_z \Upsilon^x, \; v^* = \partial_z \Upsilon^y, \; w^* = -\nabla \cdot \boldsymbol{\Upsilon}. \tag{3}$$

This corresponds to letting the antisymmetric part of **J** take the following form:

$$\frac{J - J^T}{2} = \mathrm{A} = \begin{bmatrix} 0 & 0 & \Upsilon^x \\ 0 & 0 & \Upsilon^y \\ -\Upsilon^x & -\Upsilon^y & 0 \end{bmatrix}. \tag{4}$$

(Note that generally one needs three degrees of freedom for an antisymmetric 3×3 matrix; in this case, gauge freedom implies that two degrees, i.e., the two functions Υ^x and Υ^y, are sufficient.) The GM parameterization relates $\boldsymbol{\Upsilon}$ to the isopycnal slope $\boldsymbol{s} = -\nabla_\perp \bar{\rho} / \partial_z \bar{\rho}$ through a 2×2 matrix **K**:

$$\boldsymbol{\Upsilon} = K \boldsymbol{s}, \tag{5}$$

where $\nabla_\perp = (\partial_x, \partial_y)$. The original GM parameterization uses $\mathbf{K} = \kappa \mathrm{I}$, where κ is a scalar transport coefficient. The diagonal structure of **K** implies equal ("isotropic") transport in both coordinate directions, thus differing from the more general "anisotropic" case with non-diagonal **K**. Smith and Gent (2004) argued that **K** should be symmetric and positive definite, in which case it can be shown that the parameterization mimicks baroclinic instability by removing resolved potential energy. (It bears noting that the parameterization remains advective even when **K** is not symmetric and removes resolved potential energy as long as the symmetric part of **K** is positive definite.) The parameterization presented so far does not ensure $w^* = 0$ at the ocean surface or floor and is commonly supplemented either by methods to taper the slope $\boldsymbol{s}$ to zero (Danabasoglu & McWilliams, 1995; Gerdes et al., 1991; Large et al., 1997) or to taper $\boldsymbol{\Upsilon}$ to zero (Ferrari et al., 2010).

The object of the current research is to estimate the matrix **K** using data from a global ocean circulation model simulation at eddying (0.1°) resolution, with the particular aim of providing a parameterization for its vertical structure. The horizontal structure of the anisotropic GM **K** matrix is of interest and has been targeted (along with anisotropic Redi) in recent work by Bachman et al. (2020) but is outside the scope of the present investigation. The approach taken here is to focus on the SGS eddy potential density flux $\boldsymbol{F}_\rho$ because there is no diffusion of potential density along surfaces of constant potential density, that is, the SGS eddy density flux can be completely identified with the advective, GM component of the combined GM/Redi parameterization. In the GM parameterization the horizontal part of this flux takes the simple form

$$\boldsymbol{F}_\rho = -\mathbf{K} \nabla_\perp \bar{\rho}. \tag{6}$$

Even when both $\boldsymbol{F}_\rho$ and $\nabla_\perp \bar{\rho}$ are known, it is still not possible to unambiguously solve for **K** for the simple reason that there are two equations for three unknowns. The theory of turbulent diffusion (Taylor, 1921; Vallis, 2017, Chapter 10) suggests that (2) will be a good model taken *on average*, and both theoretical and diagnostic investigations have relied on a variety of averages that are conceptually distinct from, and often used in lieu of, the spatial filter used to define large and small scales, including time averages (McDougall & McIntosh, 1996), zonal averages (Andrews & Mcintyre, 1976), averages over multiple tracers (Bachman & Fox-Kemper, 2013; Bachman et al., 2015), and averages over an ensemble of Lagrangian trajectories (Dukowicz & Smith, 1997; Monin & Yaglom, 2007). The relationship between different kinds of averaging has been explored in a channel model by Abernathey et al. (2013). The approach taken here is to use a form of averaging over depth, as described in more detail in section 2.4. Briefly, instead of allowing arbitrary vertical structure for **K**, we prescribe an a priori vertical structure and then at each horizontal location we

choose the amplitude and horizontal structure of **K** to minimize the squared difference between the model and data integrated over depth. The resulting best fit for **K** can vary arbitrarily in the horizontal and in time but has a prescribed vertical structure. An important aspect of our work is that after obtaining a fit for **K**, we also measure and report the error in the fit, that is, in how well $-\mathbf{K}\nabla_\perp\overline{\rho}$ matches $\boldsymbol{F}_\rho$. We perform this fit using various different kinds of vertical structure for **K**, which allows us to test how well the different vertical structures match the data. As a means of motivating and understanding the vertical structure of **K**, we begin by studying the vertical structure of $\boldsymbol{u}'$ and ρ', since these determine the vertical structure of $\boldsymbol{F}_\rho$ and thereby indirectly determine the structure of **K**, though the vertical structure of eddy velocity and potential density anomalies are also of interest in their own right.

The data and diagnostics applied to the data are described in section 2. Results on the vertical structure of eddy velocity $\boldsymbol{u}'$, eddy potential density ρ', and the GM coefficient **K** are presented in section 3. The results are discussed and conclusions are offered in section 4.

2. Data and Diagnostic Methods

2.1. Model Configuration

Our diagnostics are based on a nominal-0.1° POP2 ocean model simulation described by Johnson et al. (2016). The ocean and ice components are forced in accordance with the Coordinated Ocean-Ice Reference Experiments (CORE) guidelines (Griffies et al., 2009). The model is spun up for 15 years using the CORE normal-year forcing. Next, the simulation continues for 33 years using the CORE interannually varying forcing corresponding to the years 1977–2009. The output over these last 33 years is saved as 5-day averages; the last 5 years of data are used in this investigation. For each year, we use 14 time points: every 25 days starting on January 25 of each year. The data do not change much from one 5-day average to the next, so this "thinning" of the data improves the independence among the samples, making the statistics more robust.

Analysis is restricted to latitudes between 6.2°S and 64°S, avoiding both the equator and weakly stratified regions around Antarctica. The classical ideas of quasigeostrophic baroclinic instability that underpin the GM parameterization are not applicable near the equator and in weakly stratified regions. Analysis is also restricted to locations with at least 2-km ocean depth and to locations that are at least 200 grid points (approximately 2°) from shore. This is an attempt to minimize the impact of topographically locked boundary currents that occur near seamounts and continental shelves.

2.2. Spatial Filter

The first and fundamental operation applied to the data is a moving-average spatial filter. This spatial filter corresponds to a Gaussian moving average

$$\overline{u}(\boldsymbol{x}) = \int k(\boldsymbol{x},\boldsymbol{x}')u(\boldsymbol{x}')\mathrm{d}\boldsymbol{x}', \tag{7}$$

where $\boldsymbol{x} = (x, y)$, $\boldsymbol{x}'$ is a dummy integration variable, and the integral is over the horizontal domain. Eddy quantities are denoted with a $'$ and are defined as $u' = u - \overline{u}$. The Gaussian kernel used here has the form

$$k(\boldsymbol{x},\boldsymbol{x}') = \frac{1}{Z}\exp\left\{-\frac{1}{2}\left(\frac{d(\boldsymbol{x},\boldsymbol{x}')^2}{r^2}\right)\right\}\boldsymbol{I}_A(\boldsymbol{x}'), \tag{8}$$

where r is the width and Z is a normalization constant so that the kernel integrates to 1. The term $\boldsymbol{I}_A(\boldsymbol{x}')$ is an indicator function that is zero over land and one over the ocean; for computational convenience, the kernel is also truncated to zero for distances d greater than 120 grid points in the meridional direction and 180 grid points in the zonal direction. This wide truncation is required at high latitudes where the grid is smaller than the nominal 0.1° resolution suggests. The integral (7) is defined using a Cartesian tangent plane approximation centered at $\boldsymbol{x}' = \boldsymbol{x}$. On this tangent plane, the distance is defined with respect to latitude θ and longitude φ as

$$R_E\left((\theta-\theta')^2 + \frac{(\varphi-\varphi')^2}{\cos^2(\theta)}\right)^{1/2}, \tag{9}$$

where R_E is the radius of the Earth. This spatial filter does not commute with derivatives and is not appropriate for analyzing energy budgets; more sophisticated methods are required for such applications (Aluie, 2019). The GM parameterization is primarily used in ocean models that do not resolve mesoscale eddies, so

it is appropriate to choose a filter width that ensures that mesoscales are smaller than the filter scale. The deformation radius and the length scale of mesoscale eddies both vary significantly over the globe (Chelton et al., 2011; Smith, 2007), but both are typically smaller than 1° to 2° latitude. Ocean models with as small as 0.5° do not resolve mesoscale eddies, so the analysis is performed with filter widths of $r = 1\,°, 4/3°$, and 2°, where the distances are measured in degrees of latitude. This range is intended to be both representative of the resolving power of typical non-eddying models and also to be large enough to filter out the mesoscale over most of the globe. The results are insensitive to filter width over this range of r, so results are only presented for $r = 4/3\,°$.

2.3. Vertical Modes

We wish to represent the vertical structure of various quantities like $\boldsymbol{u}'$ using a small number of modes. The standard baroclinic modes are eigenfunctions of the quasigeostrophic (QG) potential vorticity (PV) stretching operator:

$$\frac{\mathrm{d}}{\mathrm{d}z}\left[\frac{f^2}{N^2}\frac{\mathrm{d}\psi_i}{\mathrm{d}z}\right] = -k_i^2\psi_i,\ \frac{\mathrm{d}\psi_i}{\mathrm{d}z} = 0 \text{ at } z = -H, 0, \tag{10}$$

where f is the local Coriolis parameter, N is the Brunt-Väisälä frequency, H is the depth, and $-k_i^2$ is the eigenvalue. The deformation radii are conventionally defined as $1/k_i$; for example, $1/k_1$ is the first baroclinic deformation radius. The barotropic mode is $\psi_0 = 1$, and the first baroclinic mode is ψ_1. It is well known that the barotropic and first baroclinic modes together are able to represent the vertical structure of the eddy velocity with high accuracy (Wunsch, 1997, 1999; Wortham & Wunsch, 2014).

It has recently been proposed that an alternative set of modes with zero flow at the bottom might be useful for describing the vertical structure of eddy energy (de La Lama et al., 2016; Groeskamp et al., 2020; LaCasce, 2017; LaCasce & Groeskamp, 2020; Wortham & Wunsch, 2014). These "surface" modes satisfy a different boundary condition from the standard baroclinic modes, namely, no flow at depth:

$$\frac{\mathrm{d}}{\mathrm{d}z}\left[\frac{f^2}{N^2}\frac{\mathrm{d}\phi_i}{\mathrm{d}z}\right] = -\tilde{k}_i^2\phi_i,\ \phi_i = 0 \text{ at } z = -H,\ \frac{\mathrm{d}\phi_i}{\mathrm{d}z} = 0 \text{ at } z = 0. \tag{11}$$

These surface modes are related to the vertical structure of Rossby waves in the presence of rough topography (Bobrovich & Reznik, 1999; Tailleux & McWilliams, 2001).

The first surface mode ϕ_1 and associated eigenvalue $-\tilde{k}_1^2$ are computed here using standard finite volume approximations and an inverse power iteration (Saad, 2011). The first baroclinic mode ψ_1 and the first baroclinic deformation radius $1/k_1$ are computed using a shifted inverse power iteration with shift $-\tilde{k}_1^2$. Both iterations converge within five to 10 iterations when started from a simple linear profile. When computing N, values below $10^{-5}\,\mathrm{s}^{-1}$ are replaced by $10^{-5}\,\mathrm{s}^{-1}$.

2.4. Projecting Onto Vertical Modes

The projection of a quantity like $\boldsymbol{u}'$ onto a single vertical mode like ϕ_1 is a straightforward exercise. In the course of the work, we also occasionally project onto two modes. When the modes are orthogonal, e.g. ψ_0 and ψ_1, this is again straightforward, but when the modes are not orthogonal, for example, ψ_0 and ϕ_1, some extra care is required. In such cases, one is attempting to represent a flow variable like u' as a linear combination of two modes, for example,

$$u' = \hat{\mathrm{u}}_0\psi_0 + \hat{\mathrm{u}}_1\phi_1. \tag{12}$$

The method used here to determine the best fit is to solve a least squares problem, that is, to find $\hat{\mathrm{u}}_0$ and $\hat{\mathrm{u}}_1$ (each independent of depth) that minimize

$$\int_{-H}^{0}(u' - \hat{\mathrm{u}}_0\psi_0 - \hat{\mathrm{u}}_1\phi_1)^2\mathrm{d}z. \tag{13}$$

This least squares problem is equivalent to the following 2×2 linear system of equations:

$$\begin{bmatrix} \int_{-H}^{0}\psi_0^2\mathrm{d}z & \int_{-H}^{0}\psi_0\phi_1\mathrm{d}z \\ \int_{-H}^{0}\psi_0\phi_1\mathrm{d}z & \int_{-H}^{0}\phi_1^2\mathrm{d}z \end{bmatrix}\begin{pmatrix} \hat{\mathrm{u}}_0 \\ \hat{\mathrm{u}}_1 \end{pmatrix} = \begin{pmatrix} \int_{-H}^{0}u'\psi_0\mathrm{d}z \\ \int_{-H}^{0}u'\phi_1\mathrm{d}z \end{pmatrix}, \tag{14}$$

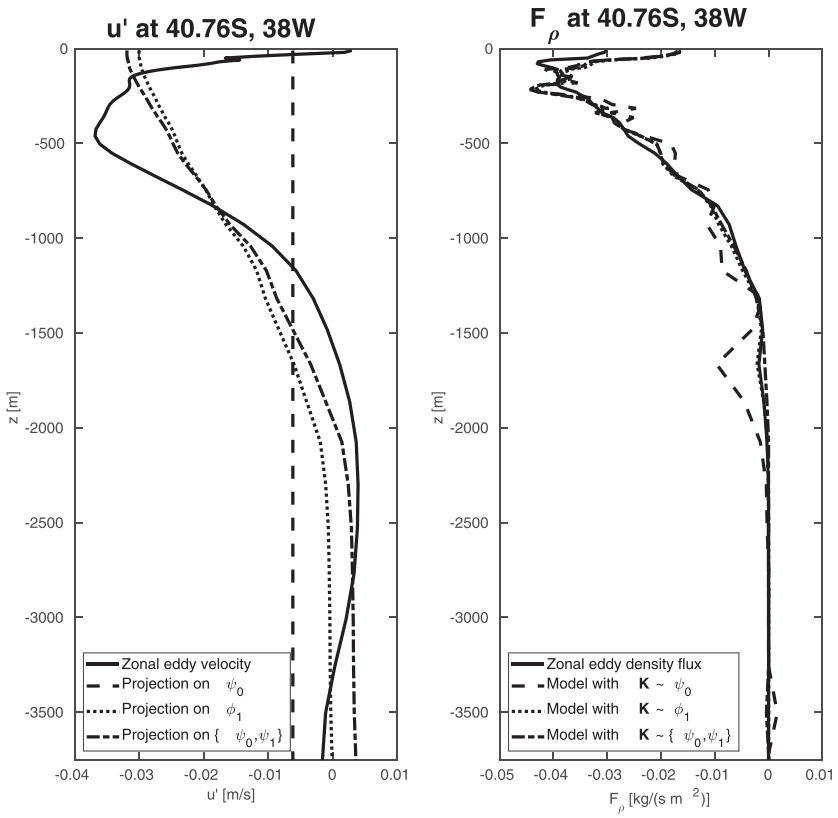

Figure 1. Left: Zonal eddy velocity u' (solid) along with projections onto ψ_0 (dashed), ϕ_1 (dotted), and simultaneous projection onto ψ_0 and ϕ_1 (dash-dot). Right: The zonal component of the eddy density flux $\mathbf{F}_\rho$ (solid) along with the flux predicted by the anisotropic GM model with $\mathbf{K}$ having vertical structure proportional to ψ_0 (dashed), ψ_1 (dotted), or a linear combination of ψ_0 and ϕ_1 (dash-dot). Both profiles were taken at 40.76°S, 38°W.

which is obtained by (i) differentiating Equation 13 with respect to $\hat{u}_0$ and setting the result to zero and (ii) differentiating Equation 13 with respect to $\hat{u}_1$ and setting the result to zero. The coefficient matrix is a Gram matrix (Olver & Shakiban, 2018, section 3.4), and the fact that ψ_0 and ϕ_1 are linearly independent (i.e., one of them is not a scalar multiple of the other) guarantees that the coefficient matrix is positive definite. The only impact of the fact that ψ_0 and ϕ_1 are not orthogonal is that the off-diagonal terms are not zero. Nevertheless, the solution always exists and is unique. Solving the least squares problem is equivalent to projecting u' onto the span of ψ_0 and ϕ_1, so for brevity, we say that we are projecting onto two modes even when the modes are not orthogonal.

A similar method is used to compute $\mathbf{K}$. The approach used here is again a least squares fit where the squared error is integrated over depth. For example, to find the best fit of $-\mathbf{K}\nabla_\perp\overline{\rho}$ to $\boldsymbol{F}_\rho$ where $\mathbf{K} = \hat{\mathbf{K}}\phi_1$ and $\hat{\mathbf{K}}$ is depth independent, we find the $\hat{\mathbf{K}}$ that minimizes

$$\int_{-H}^{0} |\boldsymbol{F}_\rho + \hat{\mathbf{K}}\phi_1\nabla_\perp\overline{\rho}|^2 \mathrm{d}z. \tag{15}$$

Similar to the discussion above, this is a linear least squares problem with a unique solution that can be found by solving a small system of equations with a symmetric and positive definite coefficient matrix.

For illustration, the vertical profile of zonal eddy velocity u' at 40.76°S, 38°W is shown in the left panel of Figure 1, along with the projections onto the barotropic mode ψ_0, the surface mode ϕ_1, and the simultaneous projections onto ψ_0 and ϕ_1 or ψ_0 and ψ_1. The vertical profile of u' changes sign three times, which suggests that at least four modes are required for an accurate fit, and for this profile, none of the fits shown is particularly good. It also illustrates the fact that the combination of the barotropic and surface modes essentially allows the surface mode to have a nonzero bottom velocity without otherwise changing the shape.

The right panel of Figure 1 shows the zonal component of the eddy density flux $\mathbf{F}_\rho$ at 40.76°S, 38°W, along with the flux generated by the anisotropic GM model with three different vertical structures: ψ_0, ϕ_1, and a linear combination of ψ_0 and ϕ_1. The fit is quite good in all cases, though the depth-independent model is clearly worse than the other two. In this example there is essentially no difference between the fit using a single vertical structure ϕ_1 for $\mathbf{K}$ and the fit using a linear combination of ψ_0 and ϕ_1.

To quantify the goodness of fit for each projection, we compute the squared relative error. For example, the squared relative error for projection of u' onto the barotropic mode ψ_0 is defined as

$$\frac{\int_{-H}^{0}(u'-\hat{u}_0\psi_0)^2 dz}{\int_{-H}^{0}(u')^2 dz}. \tag{16}$$

3. Results

3.1. Eddy Velocity

The upper panel in Figure 2 shows the root mean square (RMS) eddy velocity $|\boldsymbol{u}'|$ where the average is over depth and over 5 years. Locations with less than 2 km of depth are blacked out. The path of the Antarctic Circumpolar Current (ACC) is clearly visible, along with increased eddy kinetic energy at the Brazil/Malvinas confluence and east of Kerguelen.

The lower panels of Figure 2 show the empirical probability density function (pdf) of the squared relative error (i.e., the relative error in the eddy kinetic energy) that results from projecting $\boldsymbol{u}'$ onto various vertical structures. The projections are of poor quality in regions with very low eddy activity. To demonstrate this, empirical pdfs are constructed using data taken only from locations and times where the depth averaged RMS eddy velocity is above some threshold, and the resulting pdfs are shown as a function of the threshold. The center left panel shows the squared relative error that results from projecting onto the surface mode ϕ_1, while the center right panel shows the results of the projection onto the barotropic mode ψ_0. In both cases there is a high probability of large relative errors when all of the data are included (i.e., the threshold is zero), shown at the bottom of each panel. As the threshold increases to just a few centimeters per second, small errors become most likely. Projection onto the surface mode is clearly more accurate than projection onto the barotropic mode, since the peak of the error pdf for the surface mode projection is to the left of the peak for the barotropic mode projection.

The lower panels show the results for simultaneous projection onto the barotropic and surface modes (left) and the barotropic and first baroclinic modes (right). The use of two modes yields a massive improvement compared to one mode—the pdfs are very much concentrated on small errors—and the two different pairs of modes yield very similar results.

It is well known that the vertical structure of eddy velocity can be captured by a combination of the barotropic and first baroclinic modes (Wortham & Wunsch, 2014; Wunsch, 1997, 1999). The combination of the barotropic and first surface modes is not common and allows a clean interpretation: The barotropic mode essentially allows the structure to have a nonzero bottom velocity, while the structure on top of this bottom velocity is entirely modeled by ϕ_1. The fact that the combination of ψ_0 and ϕ_1 yields as good a fit as the combination of ψ_0 and ψ_1 implies that the primary deficiency in the surface mode ϕ_1 is the condition of no flow at depth; the vertical structure of ϕ_1 is otherwise an excellent fit. Previous investigations using the surface modes have attempted to improve the fit by projecting onto multiple surface modes ϕ_1, ϕ_2, and so on, even though all the surface modes have no flow at depth. More complete investigations of the vertical structure of eddy velocity can be found in Wortham and Wunsch (2014) and de La Lama et al. (2016); the results here are primarily intended to illuminate the results on vertical structure of the GM $\mathbf{K}$.

3.2. Eddy Potential Density

The upper panel in Figure 3 shows the RMS eddy potential density ρ' where the average is over depth and over 5 years. Locations with less than 2 km of depth are blacked out. The pattern is broadly similar to EKE, but there are exceptions, notably the region due east of Kerguelen where there is relatively more EKE than eddy potential density.

When considering the vertical structure of eddy velocity there is an abundance of theory and prior experience to guide the selection of vertical modes. The situation is less clear for eddy potential density or buoyancy anomalies. One might proceed by assuming that the dynamics are approximately geostrophic, and

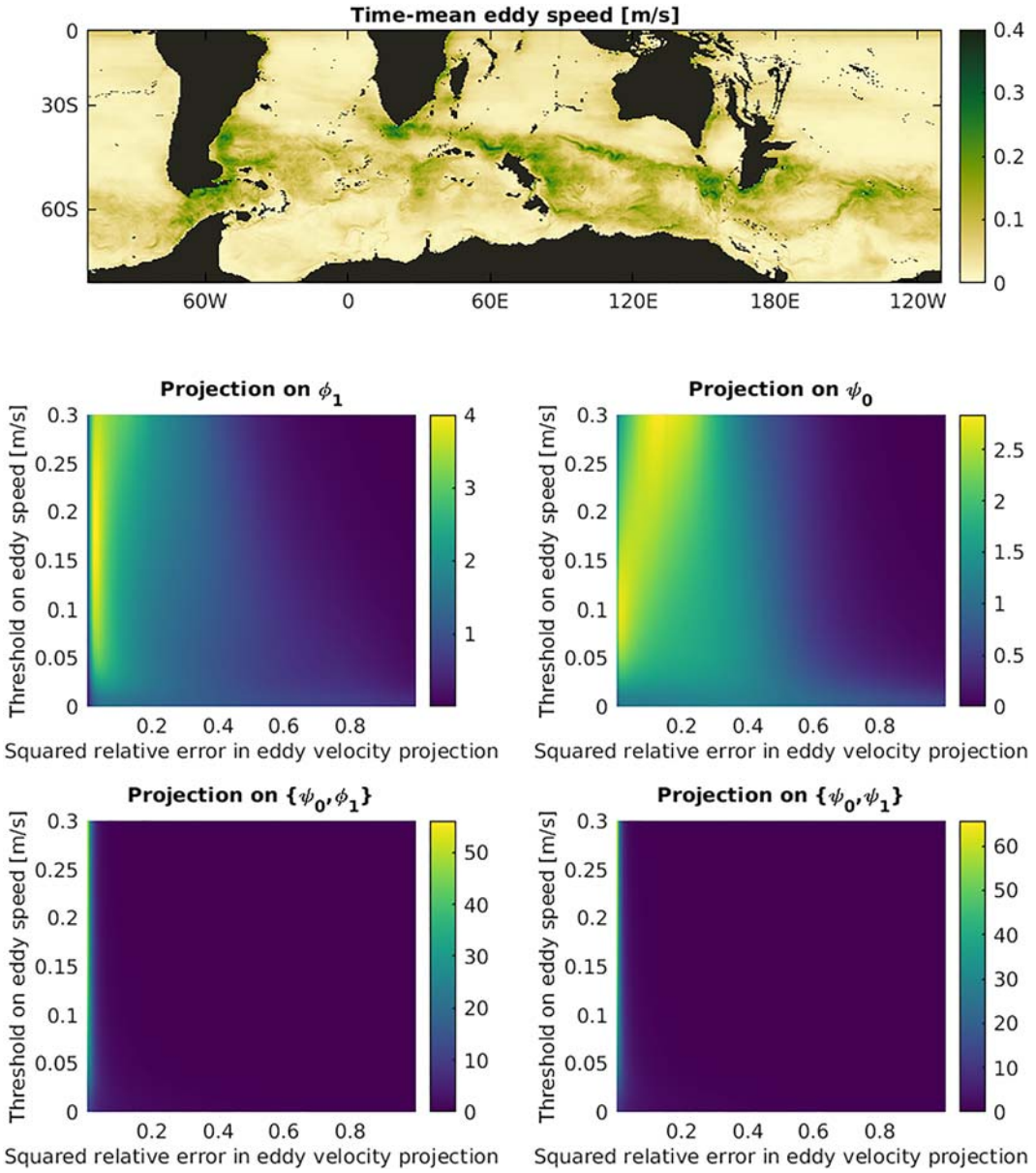

Figure 2. Top: Square root of 5-year and depth average of $|\boldsymbol{u}'|^2$ (units m/s). The four lower panels show the empirical probability density function (pdf) as a function of the data inclusion threshold. For example, a horizontal line across a panel at a y-axis value of 0.1 is the empirical pdf of the relative error only using data from locations and times with $(\int_{-H}^{0} |\mathbf{u}'|^2 \, dz)^{1/2} \geq 0.1$ m/s. Center left: Projection onto the surface mode ϕ_1. Center right: Projection onto the barotropic mode ψ_0. Lower left: Simultaneous projection onto the barotropic and surface modes. Lower right: Simultaneous projection onto the barotropic and first baroclinic (ψ_1) modes.

the results of the prior section suggest that the quasigeostrophic streamfunction ψ will be well approximated by a combination of the barotropic mode ψ_0 and either the first baroclinic mode ψ_1 or the surface mode ϕ_1. Since quasigeostrophic buoyancy is $b' = f\partial_z\psi$, one might expect that the eddy potential density ρ' should have vertical structure approximately similar to $\psi_1'(z)$ or $\phi_1'(z)$ where $'$ denotes a derivative. Unfortunately, both of these projections yield very large errors (not shown).

Mixing length theory (Vallis, 2017, Chapter 13) suggests that $\rho' \sim L|\nabla_\perp \overline{\rho}|$ where L is a mixing length. Two extremely simple models for the vertical structure of the mixing length are (i) L is depth independent and (ii) $L \propto \boldsymbol{u}'T$ where T is a depth-independent mixing time scale. As the previous section shows, the vertical structure of $\boldsymbol{u}'$ can be well approximated by the barotropic mode (which is a constant) plus either ϕ_1 or ψ_1.

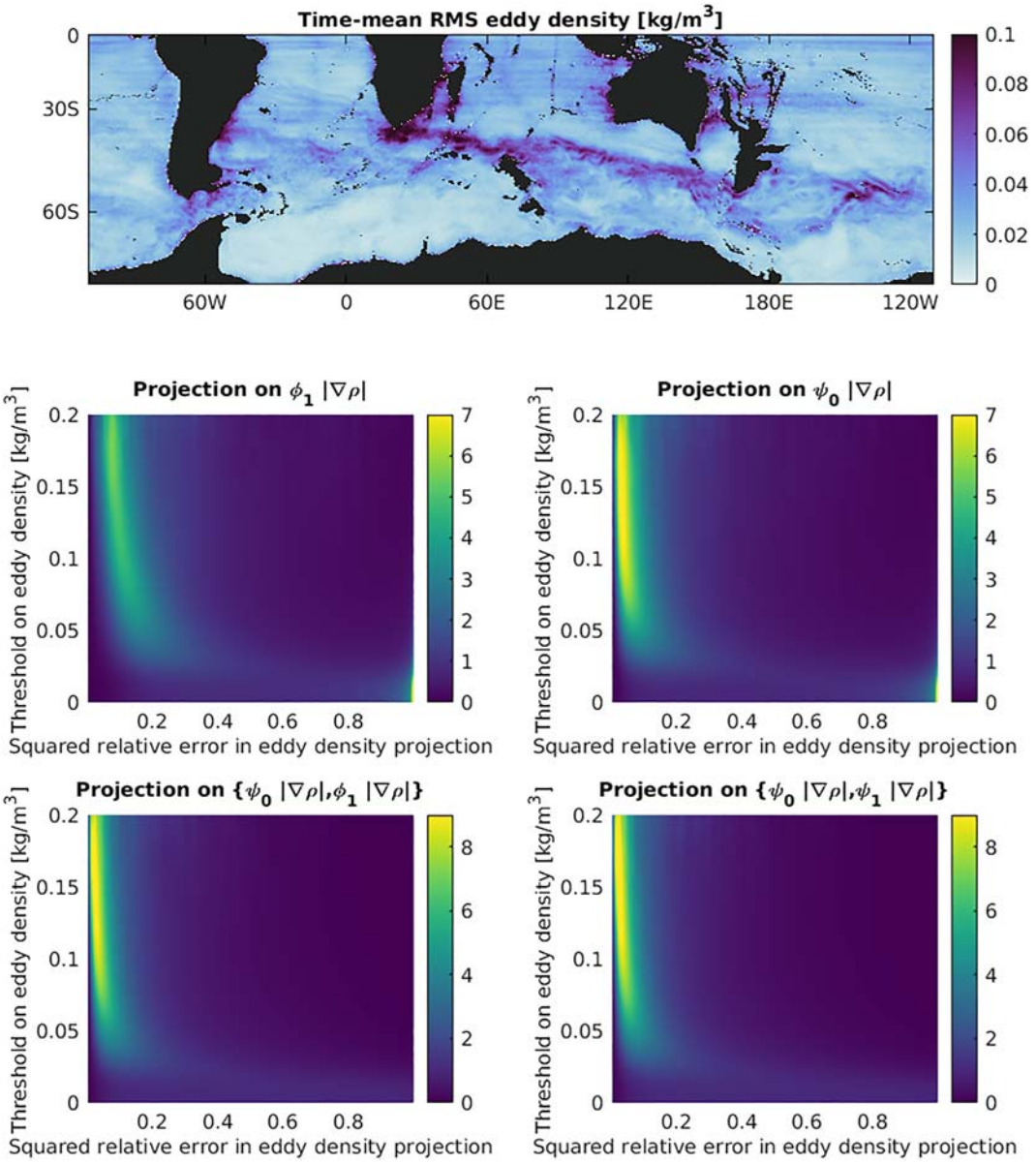

Figure 3. Top: Square root of 5-year and depth average of $(\rho')^2$ (units kg/m^3). The four lower panels show the empirical probability density function (pdf) as a function of the data inclusion threshold. For example, a horizontal line across a panel at a y-axis value of 0.1 is the empirical pdf of the relative error only using data from locations and times with $(\int_{-H}^{0}(\rho')^2\,\mathrm{d}z)^{1/2} \geq 0.1$ kg/m^3. Center left: Projection onto $\phi_1|\nabla\bar{\rho}|$. Center right: Projection onto $\psi_0|\nabla\bar{\rho}|$. Lower left: Simultaneous projection onto $\psi_0|\nabla\bar{\rho}|$ and $\phi_1|\nabla\bar{\rho}|$. Lower right: Simultaneous projection onto $\psi_0|\nabla\bar{\rho}|$ and $\psi_1|\nabla\bar{\rho}|$.

Taken together this line of reasoning suggests that the vertical structure of ρ' should be well approximated by some combination of $|\nabla_\perp\bar{\rho}|$, $\phi_1|\nabla_\perp\bar{\rho}|$, and $\psi_1|\nabla_\perp\bar{\rho}|$.

The lower panels of Figure 3 show the empirical pdf of the squared relative error that results from projecting ρ' onto various vertical structures. The projections are of poor quality in regions with very low eddy activity. To demonstrate this, empirical pdfs are constructed using data taken only from locations and times where the depth averaged RMS eddy density is above some threshold, and the resulting pdfs are shown as a function of the threshold, as in Figure 2. The center left panel shows the squared relative error that results of the projection onto $\phi_1|\nabla\bar{\rho}|$, while the center right panel shows the results of the projection onto $\psi_0|\nabla\bar{\rho}|$. In both cases, there is a high probability of large errors when all of the data are included (i.e., the threshold is zero), shown at the bottom of each panel. As the threshold increases small errors become most likely: for

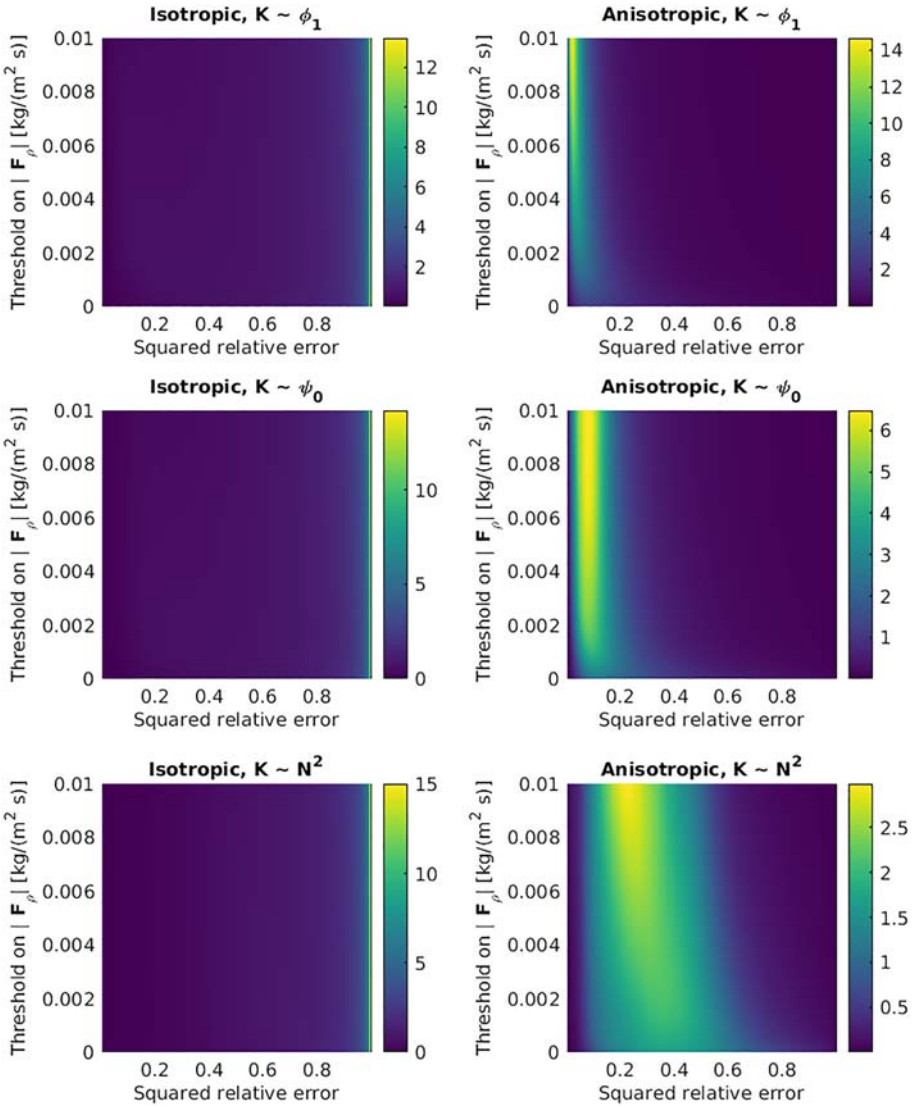

Figure 4. Left: Empirical pdfs of the squared relative error in modeling $\boldsymbol{F}_\rho$ as $-\mathbf{K}\nabla_\perp\overline{\rho}$, where the y-axis gives the data inclusion threshold. For example, a horizontal line across a panel at a y-axis value of 0.002 is the empirical pdf of the relative error only using data from locations and times with $(\int_{-H}^{0}|\boldsymbol{F}_\rho|^2\,\mathrm{d}z)^{1/2} \geq 0.002\,\mathrm{kg/m^2/s}$. The vertical structure of $\mathbf{K}$ is either ϕ_1 (top), ψ_0 (center), or N^2 (lower). Left: Isotropic $\mathbf{K} = \kappa\,\mathbf{I}$. Right: Anisotropic $\mathbf{K}$ is symmetric.

thresholds above 0.05 kg/m^3, there is a high probability of errors less than 20%. The projection onto $\psi_0|\nabla_\perp\overline{\rho}|$ is significantly better than onto $\phi_1|\nabla_\perp\overline{\rho}|$; projection onto $\psi_1|\nabla_\perp\overline{\rho}|$ is significantly worse (not shown).

The lower panels show the pdf of the squared relative error that results from simultaneous projection onto either the two profiles $\{\psi_0|\nabla_\perp\overline{\rho}|, \phi_1|\nabla_\perp\overline{\rho}|\}$ and or the two profiles $\{\psi_0|\nabla_\perp\overline{\rho}|, \psi_1|\nabla_\perp\overline{\rho}|\}$. The two models are extremely similar to each other, and they are only slightly better than projection onto $\psi_0|\nabla_\perp\overline{\rho}|$. These results are not intended to test the validity of mixing length theory; instead, the empirical vertical structure of ρ' will motivate the vertical structure of $\mathbf{K}$.

3.3. GM Coefficient

The SGS eddy potential density flux $\boldsymbol{F}_\rho$ should have a vertical structure that is similar to the product of the vertical structure of $\boldsymbol{u}'$ and ρ'. The results of section 3.1 show that $\boldsymbol{u}'$ requires at least two modes to obtain an accurate model, and that either the barotropic and surface mode, or the barotropic and first baroclinic mode will do quite well. The results of section 3.2 show that the vertical structure of ρ' can be modeled quite well with a single vertical function proportional to $|\nabla_\perp\overline{\rho}|$. Together these imply that the vertical structure of $\boldsymbol{F}_\rho$

should be well modeled as a linear combination of either $\psi_0|\nabla_\perp\overline{\rho}|$ and $\phi_1|\nabla_\perp\overline{\rho}|$ or as a linear combination of $\psi_0|\nabla_\perp\overline{\rho}|$ and $\psi_1|\nabla_\perp\overline{\rho}|$.

Rather than study the vertical structure of the flux directly, we focus on the GM approximation of the flux, namely, Equation 6. The vertical structure implied for $\boldsymbol{F}_\rho$ by the results of the previous sections suggests that the vertical structure of $\mathbf{K}$ should be well approximated by either a combination of ψ_0 and ψ_1 or a combination of ψ_0 and ϕ_1. It has also been suggested in the literature that the vertical structure of $\mathbf{K}$ should be proportional to N^2 (Danabasoglu & Marshall, 2007; Ferreira et al., 2005). Following Danabasoglu and Marshall (2007), we use the profile $N^2/N^2_{\max}$ where $N_{\max}$ is the maximal value in each column; values of $N^2/N^2_{\max}$ less than 0.1 are replaced with 0.1.

Figure 4 shows the empirical pdfs of the squared relative error that results from various parameterizations of the vertical structure of $\mathbf{K}$. The parameterizations are of poor quality in regions with very low eddy activity. To demonstrate this, empirical pdfs are constructed using data taken only from locations and times where the depth averaged RMS eddy density flux is above some threshold, and the resulting pdfs are shown as functions of the threshold, as in Figure 2. The left column shows results from the isotropic model $\mathbf{K} = \kappa\,\mathbf{I}$, while the right column shows results from the anisotropic model. The top row shows results when the vertical structure of $\mathbf{K}$ is proportional to ϕ_1; the middle row shows results when the vertical structure of $\mathbf{K}$ is proportional to ψ_0 (i.e., depth independent); and the bottom row shows results when the vertical structure of $\mathbf{K}$ is proportional to N^2.

The isotropic model produces an extremely bad fit, regardless of the vertical structure. Every panel in the left column has high probability of errors near 100%, regardless of the data inclusion threshold. In contrast, the anisotropic models are able to produce good fits to the data. The model with vertical structure proportional to ϕ_1 produces the best fit, with high probability of single-digit error percentages, while the depth-independent model is a surprisingly close runner-up with errors closer to 10%. The model with vertical structure proportional to N^2 provides a poorer fit, with high probability of errors in the range of 20–40%.

Overall these results demonstrate that a symmetric, anisotropic $\mathbf{K}$ with a single vertical structure proportional to the surface mode ϕ_1 is able to produce a very accurate model of the instantaneous SGS eddy potential density flux $\boldsymbol{F}_\rho$. The results of foregoing sections suggested that $\mathbf{K}$ would require two vertical modes: barotropic and ϕ_1 or barotropic and ψ_1. The relative success of the model with a single vertical mode may be due to the fact that the horizontal gradient of large-scale potential density can be quite small at depth, which masks the differences between a vertical structure for $\mathbf{K}$ that is nonzero at depth (e.g., using two modes), and a vertical structure of $\mathbf{K}$ that is zero at depth (cf. Figure 1). To put it another way, the vertical structure $\psi_0\nabla_\perp\overline{\rho}$ and $\phi_1\nabla_\perp\overline{\rho}$ may be similar enough to each other that the use of both ψ_0 and ϕ_1 as vertical structures for $\mathbf{K}$ is not significantly better than the use of just one mode. This hypothesis is supported by the left panel of Figure 4, which shows only a slight difference in performance between $\mathbf{K} \sim \psi_0$ and $\mathbf{K} \sim \phi_1$.

Grooms and Kleiber (2019) fit the horizontal structure of κ in an isotropic model with depth-independent κ and found a very similar bad fit to the data, but it was assumed that allowing non-constant vertical structure of κ, if anything, would improve the fit. The result that horizontal anisotropy is essentially required to obtain a good fit is perhaps suspect because of the fact that only the divergent part of the flux impacts the resolved-scale flow. It is entirely possible that the divergent part of the flux could be fit much more accurately with an isotropic model than the full flux.

Removing the nondivergent component of the SGS tracer flux is a delicate task, especially in a realistic model configuration, since the nondivergent component is not uniquely defined (Fox-Kemper et al., 2003). Some investigations have concluded that the rotational component of the tracer flux can be quite large (Bryan et al., 1999). Some previous authors have directly attempted to remove the divergent component using an isotropic model (Eden et al., 2007), while others have addressed the issue by dealing with the divergence of the flux directly in simple box geometries (Grooms & Kleiber, 2019; Mak et al., 2016). Further experiments are warranted to test whether anisotropy is indeed crucial, or whether it is merely an artifact of the divergent component of the flux; such experiments could be performed in an idealized geometry to facilitate removal of the divergent part of the eddy flux.

Though the horizontal structure of $\mathbf{K}$ is not the focus of this investigation, we offer the following brief preliminary results for the case where the vertical structure is proportional to ϕ_1. The eigenvalues of $\mathbf{K}$ appear to come in positive/negative pairs of approximately equal magnitude, as also observed recently for

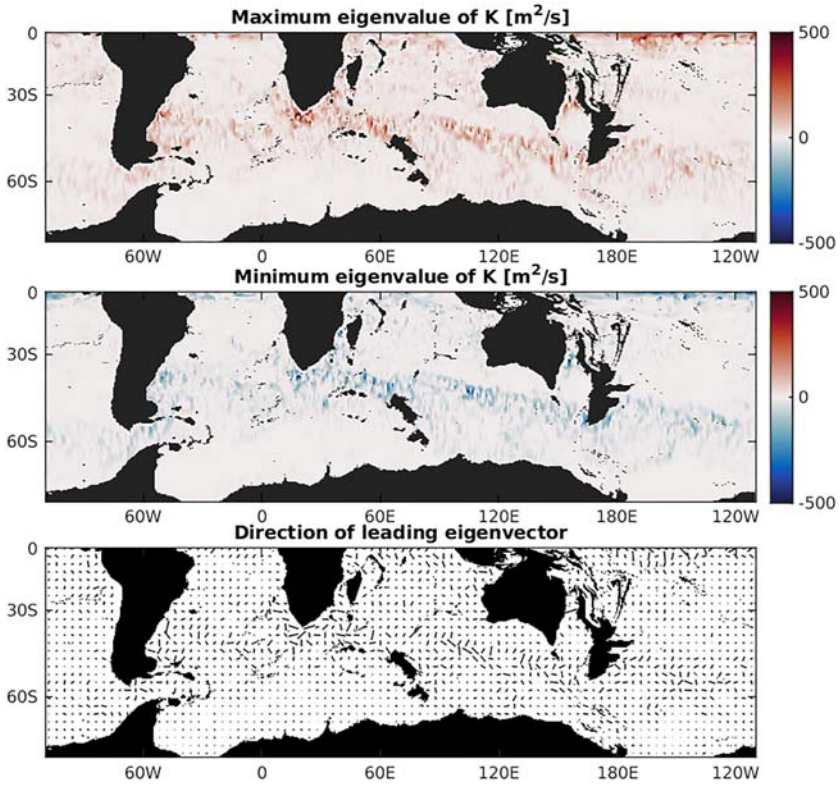

Figure 5. Horizontal structure of **K** estimated using the anisotropic model and a depth structure proportional to ϕ_1. Top: Maximal eigenvalue of **K**. Middle: Minimal eigenvalue of **K**. Bottom: Direction of the eigenvector corresponding to the maximal eigenvalue. Eigenvalue units are m^2/s.

the Redi/diffusive part of the parameterization by Haigh et al. (2020). It is not yet clear if the diffusive and anti-diffusive directions are in any way related to the large-scale flow, potential vorticity gradients, and so on. These preliminary results are illustrated in Figure 5, which shows the two eigenvalues of **K** and the direction of the leading eigenvector. **K** exhibits a large amount of spatial and temporal variability, which suggests that a stochastic model might be appropriate (Grooms, 2016; Grooms & Kleiber, 2019). This conclusion is at odds with the conclusion of Grooms and Kleiber (2019), who despaired of a stochastic parameterization of the GM coefficient on the basis of their finding that an isotropic, depth-independent GM model did not fit the data regardless of the horizontal structure of κ.

4. Conclusions

The primary conclusion to be drawn from the results in the previous section is that an anisotropic GM parameterization with coefficient **K** whose vertical structure is proportional to the surface mode ϕ_1 is able to accurately model the instantaneous SGS eddy potential density flux $\boldsymbol{F}_\rho$. The isotropic model $\mathbf{K} = \kappa\,\mathbf{I}$ is highly inaccurate, regardless of the vertical structure of κ. Progress has recently been made on specifying an anisotropic parameterization of isopycnal diffusion, that is, the Redi component of the model, by Bachman et al. (2020). Although the symmetric (Redi) and antisymmetric (GM) parts of the parameterization are conceptually distinct, they are not independent. The parameterization for the horizontal structure of isopycnal diffusion obtained by Bachman et al. (2020) could perhaps inform the horizontal structure of the GM **K** matrix. There is also a known relationship between the vertical structure of the Redi diffusivity and the GM **K** (Abernathey et al., 2013; Smith & Marshall, 2009), which could be used to lift the results here to a parameterization of the vertical structure of the Redi diffusion coefficient. Significant spatial variability in the Redi component of the transport has been noted by Abernathey and Marshall (2013) and Klocker and Abernathey (2014).

The usual caveats about rotational and divergent tracer fluxes apply here. To be specific, the GM coefficient is here fit to the full diagnosed tracer flux rather than to the divergent part of the tracer flux, whereas only

the divergent part of the tracer flux impacts the resolved scales of the tracer field. Similarly, it should be noted that the flux $\boldsymbol{F}_{\rho}$ diagnosed here contains contributions from both stationary and freely evolving eddies, whereas the GM parameterization was primarily intended to mimic free baroclinic instability. An attempt was made to reduce the impact of stationary eddies on the results by restricting attention to locations with at least 2-km depth and at least 2° from shore; nevertheless, the results still do contain contributions from stationary eddies. Stationary eddies are known to play an important role in various oceanographic processes including tracer transport (Dufour et al., 2012; Khani et al., 2019; Lu et al., 2016; MacCready & Rhines, 2001).

Data Availability Statement

Data used in this article are available at https://doi.org/10.6084/m9.figshare.12167580.v2; the scripts used to generate the data are available at https://doi.org/10.5281/zenodo.3759685.

Acknowledgments
The authors gratefully acknowledge input from three anonymous reviewers and from Steve Griffies. We are grateful to F. Bryan for providing us with the output of the simulations from (Johnson et al., 2016). I.G. is supported by National Science Foundation (NSF) OCE 1736708 and NSF OCE 1912332. Z.S. is supported by NSF OCE 1736708 and NSF DGE 1650115. S.B. is supported by NSF OCE 1912420. This material is based upon work supported by the National Center for Atmospheric Research (NCAR), which is a major facility sponsored by the National Science Foundation under Cooperative Agreement 1852977.

References

Abernathey, R., Ferreira, D., & Klocker, A. (2013). Diagnostics of isopycnal mixing in a circumpolar channel. *Ocean Modelling*, *72*, 1–16.
Abernathey, R., & Marshall, J. (2013). Global surface eddy diffusivities derived from satellite altimetry. *Journal of Geophysical Research: Oceans*, *118*, 901–916. https://doi.org/10.1002/jgrc.20066
Aluie, H. (2019). Convolutions on the sphere: Commutation with differential operators. *GEM-International Journal on Geomathematics*, *10*(1), 9.
Andrews, D. G., & Mcintyre, M. E. (1976). Planetary waves in horizontal and vertical shear: The generalized Eliassen-Palm relation and the mean zonal acceleration. *Journal of the Atmospheric Sciences*, *33*(11), 2031–2048.
Bachman, S., & Fox-Kemper, B. (2013). Eddy parameterization challenge suite I: Eady spindown. *Ocean Modelling*, *64*, 12–28.
Bachman, S. D., Fox-Kemper, B., & Bryan, F. O. (2015). A tracer-based inversion method for diagnosing eddy-induced diffusivity and advection. *Ocean Modelling*, *86*, 1–14.
Bachman, S. D., Fox-Kemper, B., & Bryan, F. O. (2020). A diagnosis of anisotropic eddy diffusion from a high-resolution global ocean model. *Journal of Advances in Modeling Earth Systems*, *12*, e21062. https://doi.org/10.1029/2019MS001904
Bachman, S. D., Fox-Kemper, B., & Pearson, B. (2017). A scale-aware subgrid model for quasi-geostrophic turbulence. *Journal of Geophysical Research: Oceans*, *122*, 1529–1554. https://doi.org/10.1002/2016JC012265
Bobrovich, A. V., & Reznik, G. M. (1999). Planetary waves in a stratified ocean of variable depth. Part 2. Continuously stratified ocean. *Journal of Fluid Mechanics*, *388*, 147–169.
Bryan, K., Dukowicz, J. K., & Smith, R. D. (1999). On the mixing coefficient in the parameterization of bolus velocity. *Journal of Physical Oceanography*, *29*(9), 2442–2456.
Chelton, D. B., Schlax, M. G., & Samelson, R. M. (2011). Global observations of nonlinear mesoscale eddies. *Progress in Oceanography*, *91*(2), 167–216.
Danabasoglu, G., & Marshall, J. (2007). Effects of vertical variations of thickness diffusivity in an ocean general circulation model. *Ocean Modelling*, *18*(2), 122–141.
Danabasoglu, G., & McWilliams, J. C. (1995). Sensitivity of the global ocean circulation to parameterizations of mesoscale tracer transports. *Journal of Climate*, *8*(12), 2967–2987.
de La Lama, M. S., LaCasce, J. H., & Fuhr, H. K. (2016). The vertical structure of ocean eddies. *Dynamics and Statistics of the Climate System*, *1*(1), dzw001.
Dufour, C. O., Le Sommer, J., Zika, J. D., Gehlen, M., Orr, J. C., Mathiot, P., & Barnier, B. (2012). Standing and transient eddies in the response of the southern ocean meridional overturning to the southern annular mode. *Journal of Climate*, *25*(20), 6958–6974.
Dukowicz, J. K., & Smith, R. D. (1997). Stochastic theory of compressible turbulent fluid transport. *Physics of Fluids*, *9*(11), 3523–3529.
Eden, C., Greatbatch, R. J., & Willebrand, J. (2007). A diagnosis of thickness fluxes in an eddy-resolving model. *Journal of Physical Oceanography*, *37*(3), 727–742.
Ferrari, R., Griffies, S. M., Nurser, A. J. G., & Vallis, G. K. (2010). A boundary-value problem for the parameterized mesoscale eddy transport. *Ocean Modelling*, *32*(3), 143–156.
Ferreira, D., Marshall, J., & Heimbach, P. (2005). Estimating eddy stresses by fitting dynamics to observations using a residual-mean ocean circulation model and its adjoint. *Journal of Physical Oceanography*, *35*(10), 1891–1910.
Fox-Kemper, B., Ferrari, R., & Pedlosky, J. (2003). On the indeterminacy of rotational and divergent eddy fluxes. *Journal of Physical Oceanography*, *33*(2), 478–483.
Fox-Kemper, B., Lumpkin, R., & Bryan, F. O. (2013). Lateral transport in the ocean interior, *International Geophysics* (vol. 103, pp. 185–209): Elsevier.
Fox-Kemper, B., & Menemenlis, D. (2008). Can large eddy simulation techniques improve mesoscale rich ocean models. *Ocean Modeling in An Eddying Regime*, *177*, 319–337.
Gent, P. R., & McWilliams, J. C. (1990). Isopycnal mixing in ocean circulation models. *Journal of Physical Oceanography*, *20*(1), 150–155.
Gent, P. R., Willebrand, J., McDougall, T. J., & McWilliams, J. C. (1995). Parameterizing eddy-induced tracer transports in ocean circulation models. *Journal of Physical Oceanography*, *25*(4), 463–474.
Gerdes, R., Köberle, C., & Willebrand, J. (1991). The influence of numerical advection schemes on the results of ocean general circulation models. *Climate Dynamics*, *5*(4), 211–226.
Griffies, S. M. (1998). The Gent-McWilliams skew flux. *Journal of Physical Oceanography*, *28*(5), 831–841.
Griffies, S. M., Biastoch, A., Böning, C., Bryan, F., Danabasoglu, G., Chassignet, E. P., et al. (2009). Coordinated ocean-ice reference experiments (COREs). *Ocean Modelling*, *26*(1-2), 1–46.
Griffies, S. M., Gnanadesikan, A., Pacanowski, R. C., Larichev, V. D., Dukowicz, J. K., & Smith, R. D. (1998). Isoneutral diffusion in a z-coordinate ocean model. *Journal of Physical Oceanography*, *28*(5), 805–830.
Groeskamp, S., LaCasce, J. H., McDougall, T. J., & Rogé, M. (2020). Full-depth global estimates of ocean mesoscale eddy mixing from observations and theory. *Geophysical Research Letters*, *47*, e2020GL089425. https://doi.org/10.1029/2020GL089425
Grooms, I. (2016). A Gaussian-product stochastic Gent-McWilliams parameterization. *Ocean Modelling*, *106*, 27–43.

Grooms, I., & Kleiber, W. (2019). Diagnosing, modeling, and testing a multiplicative stochastic Gent-McWilliams parameterization. *Ocean Modelling*, *133*, 1–10.
Haigh, M., Sun, L., Shevchenko, I., & Berloff, P. (2020). Tracer-based estimates of eddy-induced diffusivities. *Deep-Sea Research Part I*, *160*, 103,264. https://doi.org/10.1016/j.dsr.2020.103264
Hallberg, R. (2013). Using a resolution function to regulate parameterizations of oceanic mesoscale eddy effects. *Ocean Modelling*, *72*, 92–103.
Johnson, B. K., Bryan, F. O., Grodsky, S. A., & Carton, J. A. (2016). Climatological annual cycle of the salinity budgets of the subtropical maxima. *Journal of Physical Oceanography*, *46*(10), 2981–2994.
Khani, S., Jansen, M. F., & Adcroft, A. (2019). Diagnosing subgrid mesoscale eddy fluxes with and without topography. *Journal of Advances in Modeling Earth Systems*, *11*, 3995–4015. https://doi.org/10.1029/2019MS001721
Klocker, A., & Abernathey, R. (2014). Global patterns of mesoscale eddy properties and diffusivities. *Journal of Physical Oceanography*, *44*(3), 1030–1046.
LaCasce, J. H. (2017). The prevalence of oceanic surface modes. *Geophysical Research Letters*, *44*, 11,097–11,105. https://doi.org/10.1002/2017GL075430
LaCasce, J. H., & Groeskamp, S. (2020). Baroclinic modes over rough bathymetry and the surface deformation radius. *Journal of Physical Oceanography*, 1–40. https://doi.org/10.1175/jpo-d-20-0055.1
Large, W. G., Danabasoglu, G., Doney, S. C., & McWilliams, J. C. (1997). Sensitivity to surface forcing and boundary layer mixing in a global ocean model: Annual-mean climatology. *Journal of Physical Oceanography*, *27*(11), 2418–2447.
Lu, J., Wang, F., Liu, H., & Lin, P. (2016). Stationary mesoscale eddies, upgradient eddy fluxes, and the anisotropy of eddy diffusivity. *Geophysical Research Letters*, *43*, 743–751. https://doi.org/10.1002/2015GL067384
MacCready, P., & Rhines, P. B. (2001). Meridional transport across a zonal channel: Topographic localization. *Journal of Physical Oceanography*, *31*(6), 1427–1439.
Mak, J., Maddison, J. R., & Marshall, D. P. (2016). A new gauge-invariant method for diagnosing eddy diffusivities. *Ocean Modelling*, *104*, 252–268.
McDougall, T. J. (1987). Neutral surfaces. *Journal of Physical Oceanography*, *17*(11), 1950–1964.
McDougall, T. J., & McIntosh, P. C. (1996). The temporal-residual-mean velocity. Part I: Derivation and the scalar conservation equations. *Journal of Physical Oceanography*, *26*(12), 2653–2665.
McWilliams, J. C. (2013). The nature and consequences of oceanic eddies. In *Ocean Modeling in an Eddying Regime*, American Geophysical Union (AGU), pp. 5–15. https://doi.org/10.1029/177GM03
Meijers, A. J. S. (2014). The southern ocean in the coupled model intercomparison project phase 5. *Philosophical Transactions of the Royal Society A*, *372*(2019), 20130296.
Monin, A. S., & Yaglom, A. M. (2007). *Statistical fluid mechanics, volume i: Mechanics of turbulence* (Dover Edition). Mineola, NY: Dover.
Nycander, J. (2011). Energy conversion, mixing energy, and neutral surfaces with a nonlinear equation of state. *Journal of Physical Oceanography*, *41*(1), 28–41.
Olver, P. J., & Shakiban, C. (2018). Inner products and norms, *Applied Linear Algebra* (pp. 129–182). Cham: Springer International Publishing. https://doi.org/10.1007/978-3-319-91041-3_3
Qiu, B., Chen, S., Klein, P., Wang, J., Torres, H., Fu, L.-L., & Menemenlis, D. (2018). Seasonality in transition scale from balanced to unbalanced motions in the world ocean. *Journal of Physical Oceanography*, *48*(3), 591–605. https://doi.org/10.1175/JPO-D-17-0169.1
Redi, M. H. (1982). Oceanic isopycnal mixing by coordinate rotation. *Journal of Physical Oceanography*, *12*(10), 1154–1158.
Saad, Y. (2011). *Numerical methods for large eigenvalue problems: Revised edition* (Vol. 66). Philadelphia, Pennsylvania: SIAM.
Smith, K. S. (2007). The geography of linear baroclinic instability in Earth's oceans. *Journal of Marine Research*, *65*(5), 655–683.
Smith, R. D., & Gent, P. R. (2004). Anisotropic Gent–McWilliams parameterization for ocean models. *Journal of Physical Oceanography*, *34*(11), 2541–2564.
Smith, K. S., & Marshall, J. (2009). Evidence for enhanced eddy mixing at middepth in the Southern Ocean. *Journal of Physical Oceanography*, *39*(1), 50–69.
Tailleux, R., & McWilliams, J. C. (2001). The effect of bottom pressure decoupling on the speed of extratropical, baroclinic Rossby waves. *Journal of Physical Oceanography*, *31*(6), 1461–1476.
Taylor, G. I. (1921). Diffusion by continuous movements. *Proceedings of the London Mathematical Society*, *20*, 196–212.
Vallis, G. K. (2017). *Atmospheric and oceanic fluid dynamics*. Cambridge, UK: Cambridge University Press.
Visbeck, M., Marshall, J., Haine, T., & Spall, M. (1997). Specification of eddy transfer coefficients in coarse-resolution ocean circulation models. *Journal of Physical Oceanography*, *27*(3), 381–402.
Wortham, C., & Wunsch, C. (2014). A multidimensional spectral description of ocean variability. *Journal of Physical Oceanography*, *44*(3), 944–966.
Wunsch, C. (1997). The vertical partition of oceanic horizontal kinetic energy. *Journal of Physical Oceanography*, *27*(8), 1770–1794.
Wunsch, C. (1999). A summary of north atlantic baroclinic variability. *Journal of Physical Oceanography*, *29*(12), 3161–3166.
Young, W. R. (2010). Dynamic enthalpy, conservative temperature, and the seawater Boussinesq approximation. *Journal of Physical Oceanography*, *40*(2), 394–400.